

# The GTC exoplanet transit spectroscopy survey

## XI. Possible detection of Rayleigh scattering in the atmosphere of the Saturn-mass planet WASP-69b

F. Murgas<sup>1,2</sup>, G. Chen<sup>3</sup>, L. Nortmann<sup>1,2</sup>, E. Pallé<sup>1,2</sup>, and G. Nowak<sup>1,2</sup>

<sup>1</sup> Instituto de Astrofísica de Canarias (IAC), 38205 La Laguna, Tenerife, Spain  
e-mail: fmurgas@iac.es

<sup>2</sup> Departamento de Astrofísica, Universidad de La Laguna (ULL), 38206 La Laguna, Tenerife, Spain

<sup>3</sup> Key Laboratory of Planetary Sciences, Purple Mountain Observatory, Chinese Academy of Sciences, Nanjing 210008, China

Received / Accepted

### ABSTRACT

**Context.** One of the major atmospheric features in exoplanet atmospheres, detectable both from ground- and space-based facilities, is Rayleigh scattering. In hydrogen-dominated planetary atmospheres Rayleigh scattering causes the measured planetary radius to increase towards blue wavelengths in the optical range.

**Aims.** We aim to detect and improve our understanding of several features in the optical range observable in planetary atmospheres. We focus on studying transiting exoplanets that present a wide range of orbital periods, masses, radii, and irradiation from their host star.

**Methods.** We obtained a spectrophotometric time series of one transit of the Saturn-mass planet WASP-69b using the OSIRIS instrument at the Gran Telescopio Canarias. From the data we construct 19 spectroscopic transit light curves representing 20 nm wide wavelength bins spanning from 515 nm - 905 nm. We derive the transit depth for each curve individually by fitting an analytical model together with a Gaussian Processes to account for systematic noise in the light curves.

**Results.** We find that the transit depth increases towards bluer wavelengths, indicative of a larger effective planet radius. Our results are consistent with space-based measurements obtained in the near infrared using the Hubble Space telescope, which show a compatible slope of the transmission spectrum. We discuss the origin of the detected slope and argue between two possible scenarios: a Rayleigh scattering detection originating in the planet's atmosphere or a stellar activity induced signal from the host star.

**Key words.** Planets and satellites: individual: WASP-69b – planetary systems – techniques: spectroscopy – planets and satellites: atmospheres

### 1. Introduction

An active field of exoplanet science is the characterization of atmospheres of transiting planets. Due to their favorable orbital configuration and chance alignment with our line of sight, transiting planets allow us to study their atmospheres to search for atmospheric features and probe their compositions. Transmission spectroscopy has become a successful tool to study the upper layers of planetary atmospheres near the terminator region during transit (e.g., [Charbonneau et al. 2002](#), [Redfield et al. 2008](#), [Wood et al. 2011](#), [Sing et al. 2012](#), [Chen et al. 2017b](#)). In the past decade such studies were conducted for a number of planets, many of which were revealed to possess cloudy and hazy atmospheres (e.g., [Sing et al. 2011](#), [Kreidberg et al. 2014](#)). These cloudy/hazy planets reveal themselves in the form of either flat spectra, which are most likely explained by high cloud decks, or by sloped transmission spectra, with larger absorption towards shorter wavelengths (e.g., [Lecavelier Des Etangs et al. 2008](#), [Jordán et al. 2013](#)). Coupled with muted molecular features these sloped spectra are best explained by photochemical hazes in the atmosphere (e.g., [Sing et al. 2016](#)) or by atmospheric Rayleigh scattering. While high-resolution transmission studies are probing individual lines (e.g., [Wyttenbach et al. 2017](#), [Casasayas-Barris et al. 2018](#), [Seidel et al. 2019](#),

[Casasayas-Barris et al. 2019](#), [Chen et al. 2020](#)), studies at lower resolution can give us information about the continuum of the exoplanet spectrum (e.g., [Rackham et al. 2017](#), [May et al. 2018](#), [Bixel et al. 2019](#), [Todorov et al. 2019](#), [May et al. 2020](#), [Weaver et al. 2020](#)). Moreover, ground and space-based low resolution transmission spectroscopy allows us to probe for potential broad absorption line wings and slopes caused by hazes in the atmosphere of Jovian-like transiting planets. The presence of broad absorption lines and/or slopes at optical wavelengths and water absorption bands in the near-infrared can help us to break the degeneracy between the atmospheric pressure and abundances of elements using spectral retrieval analysis techniques (e.g., [Benneke & Seager 2012](#), [Heng & Kitzmann 2017](#)). Hence, having a library of ground or space-based optical and near-infrared observations can help to establish abundances of transiting planets using current facilities like HST/WFC3 or complement future observations made with JWST.

Here we report the analysis of one planetary transit of WASP-69b obtained with the OSIRIS instrument (Optical System for Imaging and low-Intermediate-Resolution Integrated Spectroscopy; [Sánchez et al. 2012](#)) mounted on the 10.4 m Gran Telescopio Canarias (GTC). WASP-69b is a Saturn-mass ( $0.26 M_{\text{Jup}}$ ) highly inflated ( $1.06 R_{\text{Jup}}$ ) planet orbiting a K-type star with a period of approximately 3.9 days ([Anderson et al. 2014](#)).

The planet is of special interest due to its low mean density and as it has been shown to lose its atmosphere in form of a tail through studies of its near infrared helium signature (Nortmann et al. 2018). Using WFC3 on the Hubble Space Telescope the planet was found to have a muted water feature at  $1.4 \mu\text{m}$  with an overlying slope of larger planet radius towards bluer wavelengths (Tsiaras et al. 2018). Further, absorption in Na D was detected during transit using high resolution observations obtained with the HARPS spectrograph (Casasayas-Barris et al. 2017), although an independent study using ESPaDOnS/CFHT could not confirm the sodium detection (Deibert et al. 2019).

This paper is organized as follows. In Sect. 2 we present the observations and data reduction strategy. In Sect. 3 we describe our light curve fitting procedure. In Sect. 4 and 5 we present our optical WASP-69b transmission spectrum and joint analysis of our results and a published near infrared transmission spectrum of the planet. In Sect. 6 we present the conclusions of this work.

## 2. Data observations and reduction

### 2.1. Observing setup

The observations were taken on 5th October 2016 using the OSIRIS spectrograph on the GTC (Cepa et al. 2000) in long-slit spectroscopy mode. For this the planet host star and a reference star of similar brightness (see Table 1 for coordinates and magnitude information) were both placed in the slit (see Fig. 1). The slit was 40 arc second wide and custom-build for exoplanet atmosphere observations. The width of the slit allows to minimize possible flux losses in case of seeing variability or small position drifts of the star within the slit during the observations. The observations were done using the R1000R grism, covering the wavelength range 510 - 905 (redder wavelength up to 1000 nm are covered but heavily affected by fringing and are thus discarded). The observations were started at 20:23 UT, 49 min before the transit ingress, and lasted for 3h 36 min, ending at 00:00, 34 min after the transit egress. The observations were stopped prematurely due to a problem with the Data Acquisition System (DAS). The individual exposure times were set to 4 s, which yielded 591 spectra in total (367 during transit and 223 out of transit). At the beginning of the observations the airmass was 1.6 and towards the end 1.23. The average seeing was 1.7 arcsec. A  $2 \times 2$  binning was used, the gain was  $1.46 e^-/\text{ADU}$ , the readout speed was 500 KHz, and the readout noise was  $8.0 e^-$ .

### 2.2. Data reduction

The data were reduced following the approach described by Chen et al. (2017a) taking into account overscan, bias, flat field and sky background correction. For the wavelength calibration we made use of the full 2D information of the arc lamp exposures to create a pixel to wavelength transformation map. This assured the correct wavelength calibration for each obtained spectra even in case the position of the spectral trace changes in each exposure. The spectra are extracted along the spectral trace using the optimal extraction algorithm (Horne 1986). We tested several extraction apertures and compared the out-of-transit point to point scatter of the light curve. The lowest scatter was found when we use a fixed aperture of 42 pixels for both target and reference star and we adopt this aperture for the following analysis. Time stamps for every spectrum were calculated to correspond to the middle of the exposure and converted into the Barycentric Julian Date in Barycentric Dynamical Time standard following Eastman et al. (2010). To create light curves for both stars the flux

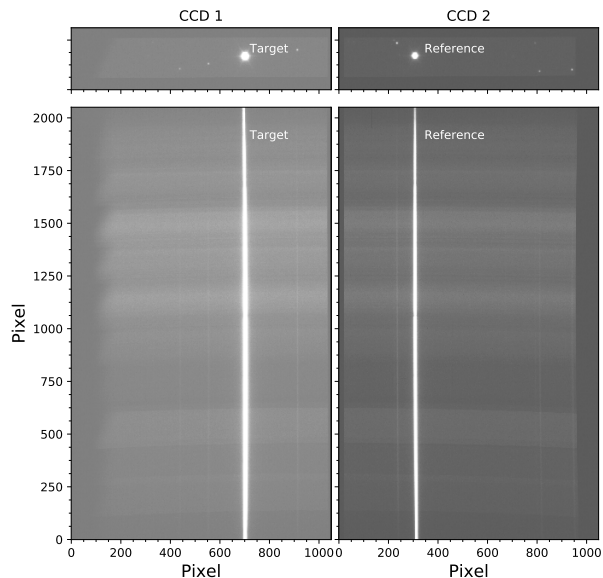


**Fig. 1.** *Top panel:* Through slit image of the target WASP-69 and the reference star in imaging mode of GTC/OSIRIS. WASP-69 was placed in CCD 1 and the reference star was placed in CCD 2. *Bottom panel:* Raw science image after activating spectroscopy mode.

in each spectrum was integrated over a given pass band. For the white light curve the flux was integrated over the range 515 - 905 nm, excluding the region of low flux caused by the strong oxygen absorption band between 757 - 768 nm. In order to correct effects of variable telluric absorption, seeing and atmospheric extinction over the course of the observation the absolute light curve of the target star, WASP-69, is divided by the absolute light curve of the reference star to create a relative light curve. In Fig. 2 we show the absolute light curves of both stars together with the relative transit light curve.

To calculate relative light curves for 19 spectroscopic channels the spectral range is divided into 20 nm wide bins. These bins are indicated in Fig. 3 for spectra of both stars. For each 20 nm wide interval the process described for the creation of a white light curve was repeated using a narrower wavelength interval. The resulting spectroscopic light curves are shown in Fig. 4.

## 3. Data Analysis

### 3.1. White light curve

In order to derive the wavelength independent transit parameters and fix them in the subsequent analysis of the spectroscopic light curve analysis we fitted the white light curve (see Chen et al. 2018 for details). For the fitting process we use the python package batman (Kreidberg 2015), which describes the transit light curve using the analytical model by Mandel & Agol (2002). We account for systematic trends (red noise) in the light curves using Gaussian Processes (GP; Rasmussen & Williams 2010, Gibson et al. 2012, Ambikasaran et al. 2015). The major sources of red noise that we considered in our modeling were the seeing variation (measured by the FWHM of the spatial profile), the position of the target star along the spatial direction, and a time component. These vectors were then used as input to a squared expo-

**Table 1.** Coordinates of the planet host star WASP-69 and the reference star used in the observing run.

Star	2MASS ID	RA *	Dec *	$V_{\text{mag}}$	$(B - V)_{\text{mag}}$
WASP-69	J21000618-0505398	20h 00m 05.20s	−05° 05′ 40.037″	9.87 <sup>b</sup>	1.06 <sup>b</sup>
Reference	J20595897-0507535	20h 59m 59.00s	−05° 07′ 53.766″	10.60 <sup>b</sup>	1.03 <sup>b</sup>

**Notes.** <sup>(a)</sup> Reference for coordinates: [Gaia Collaboration \(2018\)](#) <sup>(b)</sup> [Høg et al. \(2000\)](#)

**Table 2.** Best-fitting planet system parameters from optimization using Gaussian processes for the white light curve of WASP-69b.

Transit parameter	Value
$R_p/R_\star$	$0.13238^{+0.00091}_{-0.00094}$
$a_p/R_\star$	$12.07^{+0.203}_{-0.198}$
$T_{\text{mid}}[\text{BJD}_{\text{TBD}}]$	2457667.432296(171)
Period [d]	3.8681382 <sup>a</sup> (fixed)
$i$ (deg)	$86.692^{+0.122}_{-0.123}$
$\omega$ (deg)	90 <sup>a</sup> (fixed)
$e$	0 <sup>a</sup> (fixed)
$u_1$	$0.451^{+0.067}_{-0.067}$
$u_2$	$0.118^{+0.083}_{-0.084}$

**Notes.** <sup>(a)</sup> [Anderson et al. \(2014\)](#).

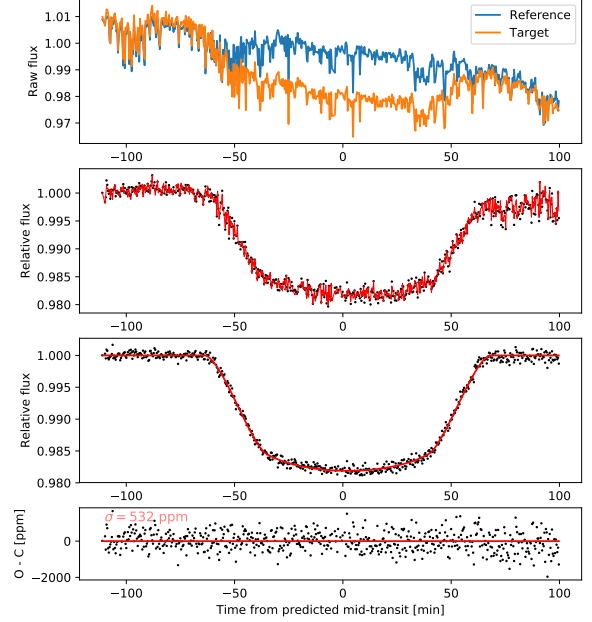


**Fig. 2.** White light transit curve of WASP-69b. *Upper panel:* raw light curve of WASP-69 (orange) and the reference star (blue), respectively. *Second panel from the top:* Relative white light curve (black points) with best fitting model (in red) including the modeled transit curve and components to model the effects of seeing and other systematic noise sources. *Third panel from the top:* Relative white light curve with the modeled noise components removed. The best fitting transit model is plotted in red. *Bottom panel:* Residuals after the best fitting model is subtracted from the data are plotted in black with a red line indicating the zero level. The scatter of the residuals is 532 ppm.

nential kernel, with the amplitude and scale of the kernel set as free parameters.

The quadratic limb darkening coefficients  $u_1$  and  $u_2$  were calculated by interpolating a stellar atmosphere model with the stellar effective temperature of the host star ( $T_{\text{eff}} = 4700$  K, surface gravity  $\log g_\star = 4.50$  and metallicity  $[\text{Fe}/\text{H}] = 0.150$  ([Anderson et al. 2014](#))) from the ATLAS synthetic models ([Kurucz 1979](#)) using the code of [Espinoza & Jordán \(2015\)](#).

In the transit light curve fit the free parameters were the planet-to-star radius ratio  $R_p/R_\star$ , the semi major axis in units of the stellar radius  $a_p/R_\star$ , the orbital inclination  $i$  and the mid-transit time  $T_{\text{mid}}$ . The period and the orbital eccentricity were fixed to the values from the discovery paper ([Anderson et al. 2014](#)) ( $e = 0$ ). The MCMC procedure consisted of 90 chains, each one with 3000 iterations. The final values and associated errors of the fitted parameters were estimated using the percentiles of the posterior distribution (median and 1- $\sigma$  uncertainties). The best fitting transit parameters for the white light curve fit are given in Table 2. The best fitting models are shown together with the data in Fig. 2.

### 3.2. Spectroscopic light curves

For the analysis of the spectroscopic light curves the wavelength independent transit parameters were fixed to the values obtained for the white light curve and only the planet-to-star radius ratio and the limb darkening coefficients were allowed to vary. We created a common-mode noise model by dividing the white light curve by the best analytical transit model fit, then we divided each individual light curve by this common-mode noise model. Next, we fitted a transit model together with a red noise model using the same inputs as the white light curve (i.e., a squared

exponential kernel with seeing, star position in spatial direction, and time component as inputs) to the spectroscopic light curves corrected by the common-mode noise model. To estimate the best-fitted parameter values and their 1- $\sigma$  uncertainties we used 32 chains running for 3000 iterations each; after that we obtained the fitted values and uncertainties from the posterior distribution of the parameters. In Figure 4 all 19 curves are shown together with the best fitting model including the GP noise model.

## 4. GTC/OSIRIS optical transmission spectrum

The resulting wavelength dependent planet-to-star radius ratio is given in Table A.1, and the resulting optical transmission spectrum of the exoplanet is plotted in Fig. 5. In that figure, the transmission spectrum is compared to two different synthetic models as well as to a Rayleigh scattering slope and a line indicating a completely flat atmospheric transmission.

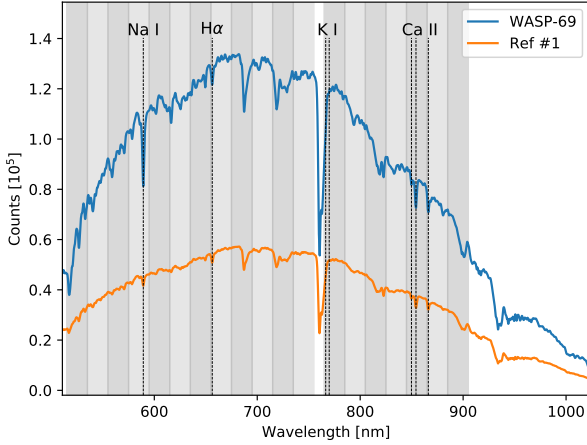


**Fig. 3.** Sample spectra of WASP-69 (blue) and the reference star (orange). Indicated in grey lines are the limits of the narrow pass bands used to create the 19 spectrophotometric light curves. The position of several strong atmospheric lines are also marked. The spectral region at 760 nm is excluded from narrow pass bands as it is strongly affected by telluric oxygen absorption introducing noise to the data.

The data show no indication of absorption by sodium or potassium, rejecting the model of a clear atmosphere with solar abundance at high confidence. Comparison of the data to a flat line also rejects a cloudy, flat transmission spectrum. Instead the data exhibit a clear trend of increasing planet radius towards shorter wavelengths. This slope is compatible with the expected increase due to Rayleigh scattering.

#### 4.1. Rayleigh scattering

The equation that predicts the change of the measured planetary radius across wavelength in a Rayleigh scattering regime is (Lecavelier Des Etangs et al. 2008):

$$\frac{dR_p}{d \ln \lambda} = \alpha H = \alpha \frac{\kappa_B T}{\mu_m g_p} \quad (1)$$

where  $H$  is the atmospheric scale height,  $\kappa_B$  the Boltzmann constant,  $T$  is the planet's atmospheric temperature,  $\mu_m$  is the mean molecular weight of the planetary atmosphere, and  $g_p$  is the surface gravity of the planet. If the particles that are causing the scattering are mainly hydrogen it is expected that  $\alpha = -4.0$ .

Assuming an hydrogen-dominated atmosphere ( $\mu_m = 2.37$ ), and an atmospheric temperature equal to the planetary equilibrium temperature ( $T_{eq} = 963 \pm 18$  K) and  $\log g_p = 2.726 \pm 0.046$  (cgs) (values taken from Anderson et al. 2014), we find  $\alpha = -3.35 \pm 0.75$ , a value consistent with the expected metrics from hydrogen.

Another indirect evidence that support the hypothesis that the observed slope is caused by hydrogen is the escaping tail of Helium discovered by Nortmann et al. (2018). If Helium has been detected in the upper atmosphere of WASP-69b it is likely that there is also a detectable amount of hydrogen in its atmosphere. However, since WASP-69 is an active star with evidence of strong emission in Ca II H+K lines ( $\log R'_{HK} \sim -4.54$ , Anderson et al. 2014) it is possible that the slope that we detect with GTC could also be caused by stellar activity.

**Table 3.** Spot modeling fit.

Parameter	Prior type and range	Fitted value
$(R_p/R_\star)$	Uniform [0.06, 0.26]	$0.12880^{+0.00042}_{-0.00041}$
$\delta_{spot}$	Uniform [0.0, 1.0]	$0.553^{+0.301}_{-0.267}$
$\delta_{facu}$	Uniform [0.0, 1.0]	$0.149^{+0.460}_{-0.132}$
$T_{phot}$	Normal [ $\mu = 4700, \sigma = 50$ ]	$4716^{+22.6}_{-33.4}$ K
$T_{spot}$	Uniform [2700, 4700]	$4594^{+48.1}_{-77.4}$ K
$T_{facu}$	Uniform [4700, 7000]	$4788^{+307.8}_{-68.2}$ K

#### 4.2. Stellar spots and faculae

As WASP-69b is an active star, the role of occulted and unocculted stellar spots and faculae and their ability to imprint themselves on the transmission spectrum needs to be taken into account. We do not detect any obvious deformation in the light curves indicative of stellar spots occulted by the planet during the observed transit. However a slope towards larger radii with short wavelength can be caused by unocculted spots on the stellar disc (e.g., Pont et al. 2013, McCullough et al. 2014, Oshagh et al. 2014). Unocculted spots can cause an increase of the apparent planet-to-star radius ratio towards the blue, due to the wavelength dependent contrast between a cold spot and remaining stellar surface which increases towards shorter wavelengths. On the other hand faculae (zones with slightly hotter temperature than the average of the star) can cause the opposite effect: an increase of the apparent planet-to-star radius ratio towards the red-der parts of the optical spectrum. A simple way to describe the expected change in apparent radius ratio is given by Eq. 2 (Rackham et al. 2018 and references therein), here  $\delta_{spot}$  and  $\delta_{facu}$  are the area ratio between the spot and faculae covered area and the entire stellar disc,  $F_v(\text{spot})$  and  $F_v(\text{facu})$  are the flux from the spots and faculae, and  $F_v(\text{phot})$  the flux of the stellar disc.

$$\left(\frac{\hat{R}_p}{\hat{R}_\star}\right)^2 = \left(\frac{R_p}{R_\star}\right)^2 \frac{1}{1 - \delta_{spot} \left(1 - \frac{F_v(\text{spot})}{F_v(\text{phot})}\right) - \delta_{facu} \left(1 - \frac{F_v(\text{facu})}{F_v(\text{phot})}\right)} \quad (2)$$

We explore this scenario by fitting the transmission spectra using a grid of PHOENIX stellar spectra (Husser et al. 2013) with different temperatures (ranging from 2700 K to 7000 K) but with the same metallicity and  $\log g_\star$  as WASP-69 (taken from Anderson et al. 2014) to model the temperature of the star, the spots, and the faculae. As described in Murgas et al. (2019), a MCMC fitting was done using emcee (Foreman-Mackey et al. 2013): we used 80 chains and a two step iteration procedure (7500 iterations as burn-in phase and 25000 iterations as the main MCMC run). The type of prior and range of values used for each parameter is presented in Table 3. After the MCMC fit was done, the best fitted values were adopted from the posterior distributions of the fitted parameters (the median from the distribution as the final parameter value and  $1\sigma$  uncertainty range as the respective error bar).

The results of the best fitting spot and faculae coverage model that is able to reproduce our observed transmission spectrum are presented in Table 3, and Figure A.1 presents the correlation plots of the fitted parameters. The model converges to a star temperature of  $T_{phot} = 4716^{+23}_{-33}$  K, a spot temperature of



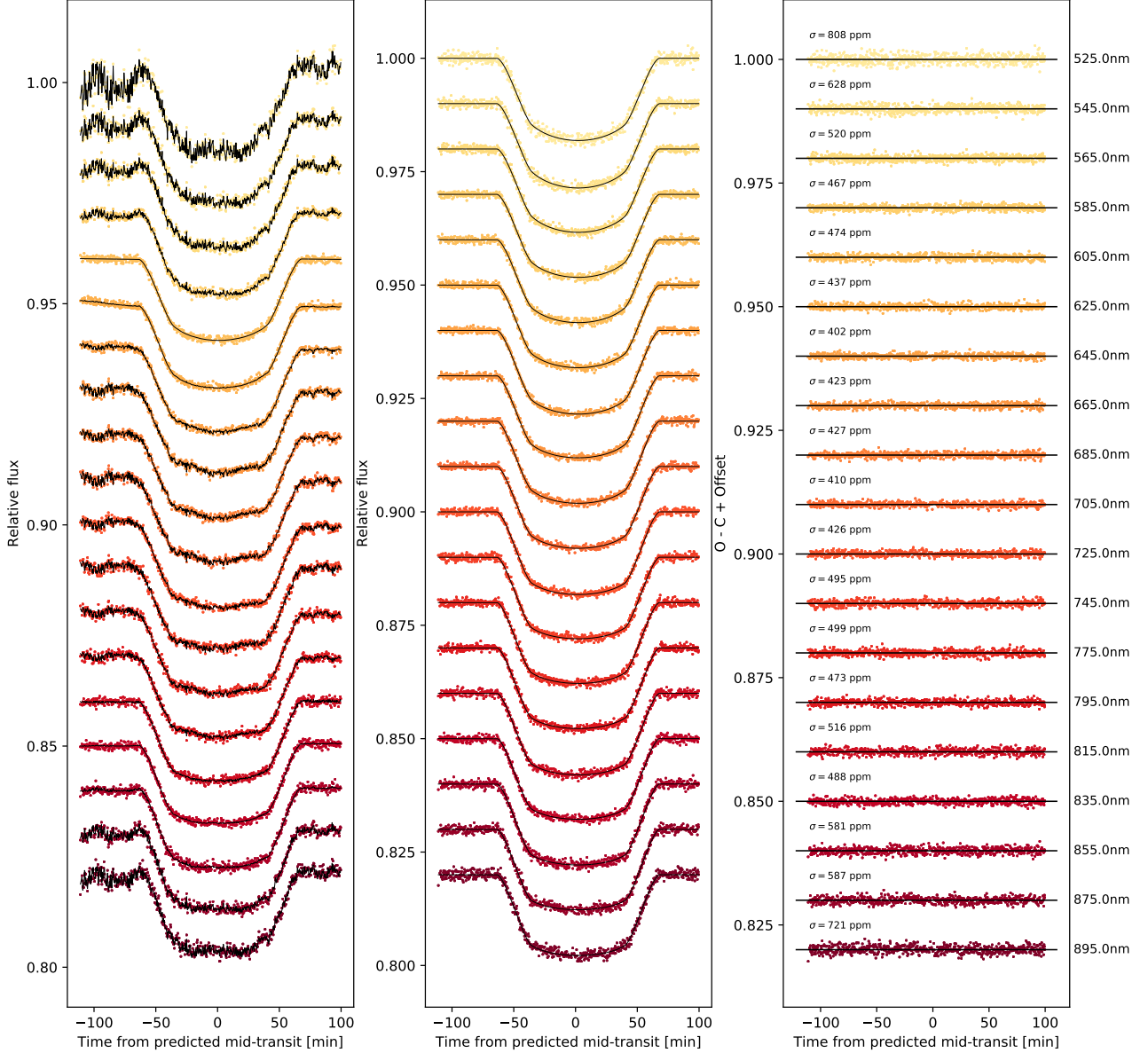


**Fig. 4.** *Left panel:* All 19 spectroscopic light curves where common-mode noise has been removed, with the respective best fitting model (including transit light curve and noise model) plotted in black. *Middle panel:* Same spectroscopic light curves after the model for systematic trends was removed. The best fitting transit model considering the red noise is plotted in black. *Right panel:* Residuals after the best fitting models were subtracted.

$T_{\text{spot}} = 4594^{+48}_{-77}$  K, and a faculae temperature of  $T_{\text{facu}} = 4788^{+308}_{-68}$  K. The temperature contrast between the stellar surface and the spots is  $\Delta T_{\text{phot-spot}} = +122$  K and the temperature contrast stellar surface versus faculae is  $\Delta T_{\text{phot-facu}} = -72$  K. The filling factors for the spots and faculae are  $\delta_{\text{spot}} = 0.55^{+0.30}_{-0.27}$  and  $\delta_{\text{facu}} = 0.15^{+0.46}_{-0.13}$ , respectively. As mentioned in Murgas et al. (2019) and references therein, for active K dwarfs spot coverage of the order of 40-50% are not rare, however the correlation plot of the fit shows that the filling factors of the spots and faculae are not well constrained, and are degenerate with the temperature of their respective features.

A combination of stellar features such as spots and faculae can explain the slope we detect with GTC, which would make the transmission spectrum of WASP-69b similar to the Neptune-sized planet HAT-P-11b. HAT-P-11b presented in one GTC ob-

servation a Rayleigh-like feature which was attributed to spots in contrast to the flat transmission spectrum observed in another occasion with the same instrument (Murgas et al. 2019). However, unlike HAT-P-11b, for WASP-69b there are no reported cases of spot regions big enough to be detected as spot crossing events in the follow up observations made in the discovery paper by Anderson et al. (2014); although there are evidences of stellar modulation due to spots in their long trend light curves. Nor do we detect any spot-crossing in our high-precision white-light photometric light curve. Future monitoring of several WASP-69b transits may help solve this issue.

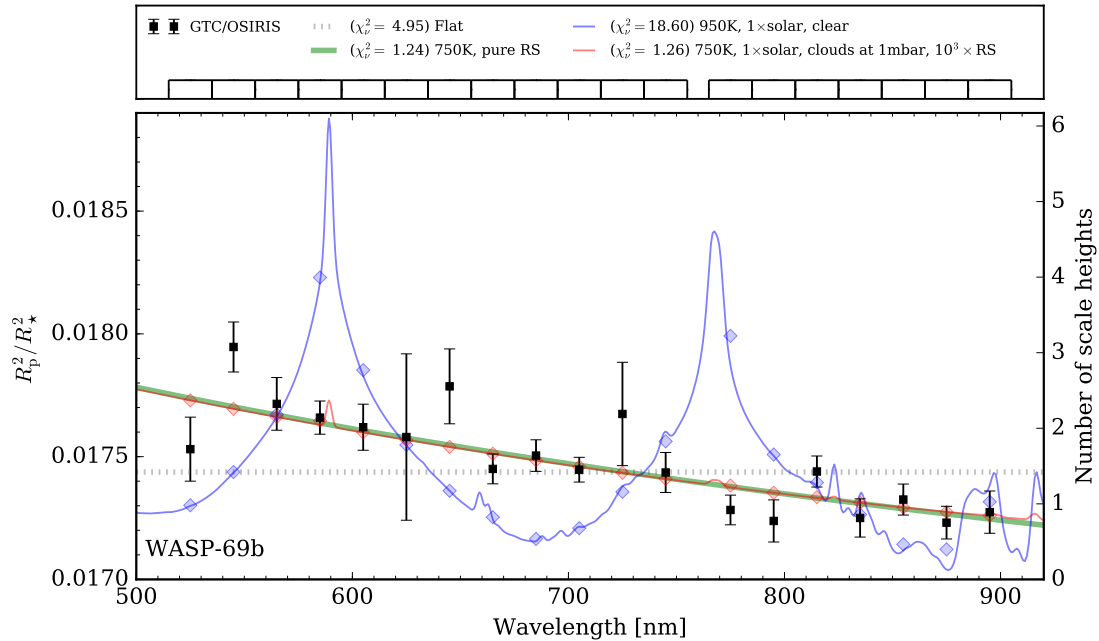


**Fig. 5.** Optical transmission spectrum of WASP-69b (black squares) compared with several theoretical atmosphere models. In blue a model created using Exo-Transmit (Kempton et al. 2017) for a clear atmosphere and solar abundance is shown. The grey dotted line indicates a the model of flat transmission spectrum. The slope expected in an atmospheres affected solely by Rayleigh scattering is shown in green. In red we show the model of an atmosphere with clouds at 1 mbar and Rayleigh scattering enhanced by a factor of 1000. *Top panel* shows the legend and the bins of bandpass to derive the transmission spectrum.

#### 4.3. Exploring the Na I doublet region for planetary absorption

Using HARPS-North high resolution spectroscopy ( $R \sim 115000$ ) Casasayas-Barris et al. (2017) reported an excess of the measured planetary radius of WASP-69b around the Na I doublet (absorption lines D2 with  $\lambda_{D2} = 589.0$  nm and D1  $\lambda_{D1} = 589.6$  nm). In contrast, Deibert et al. (2019) did not find the excess of the planetary radius around the Na I lines in their study of Warm Saturns using ESPaDOnS ( $R \sim 60000$ ) instrument on CFHT. Although low resolution transmission spectroscopy is not so sensitive to the core of absorption lines, it can still be a useful tool to detect Na in transiting planets testing the detection of broad line wings in clear atmospheres.

We explored the region around the Na I doublet using 11 spectroscopic channels of 5 nm of width to see if we are able to detect an excess of the measured planet-to-star radius ratio that confirms the presence of Na in the atmosphere of WASP-69b. Table A.2 presents the measured  $R_p/R_\star$  with their  $1\sigma$  uncertainties and Figure A.2 shows the transmission spectrum around the Na I doublet and compares the measurements with different models. We do not detect either an extra absorption in the bin centered at the Na I doublet nor the broad absorption line wings associated with a clear atmosphere (i.e., an atmosphere without clouds or hazes that mute the Na absorption signal). Casasayas-Barris et al. (2017) measured a line contrast of 5.8% for the D2 line and no detection of D1. The average seeing of  $1.9''$  corresponds to  $\sim 20$  Å for the OSIRIS observation. If we integrate the high-resolution excess absorption line profile and convolve it with the seeing-limited spectral resolution, we would measure an transit depth difference of 44 ppm in a bin width of 5 nm. This value is much smaller than our typical uncertainty of  $\sim 120$  ppm around the Na doublet (see Table A.2), hence with our GTC low res-

olution data we would not be able to detect the Na absorption presented in Casasayas-Barris et al. (2017).

As mentioned in Murgas et al. (2019), the measured planet-to-star radius ratio centered around the Na I doublet can be affected by unocculted stellar spots (for a more detailed discussion see Rackham et al. 2019). In Fig. A.2 the best fitted model that takes into account unocculted spots and faculae is shown in orange. The predicted amplitude of the Na feature produced by unocculted spots is significantly less than the amplitude predicted by planetary atmospheric models and of comparable size of the uncertainty of our measurements.

#### 5. Optical and near infrared transmission spectrum of WASP-69b

We put our transmission spectrum observed in the optical range into context by comparing them to the results obtained by Tsiaras et al. (2018) in the near infrared using WFC3 at the Hubble space Telescope (HST), as shown in Figures 6 and 7). Their results exhibit the detection of a muted water band together with a sloped continuum.

The planet ratio derived from OSIRIS transmission spectrum is higher than from the WFC3 transmission spectrum with an overall offset of  $\Delta R_p/R_\star \sim 0.00221$ . Alexoudi et al. (2018) found that different sets of orbital parameters (e.g.,  $a/R_\star$  and  $i$ ) could systematically introduce discrepancy to the transmission spectrum. In our case, if we fixed the transit parameters to the ones adopted by WFC3 (i.e.,  $a/R_\star = 11.953$  and  $i = 86.71^\circ$ ), the OSIRIS transmission spectrum would hold the same spectral shape but move downwards with an overall offset of  $\Delta R_p/R_\star = 0.00076$ , which cannot account for the observed offset of  $\Delta R_p/R_\star \sim 0.00221$ . The remaining offset could come from the bias introduced by different instrumental systematics, or different flux levels caused by the modulation of stellar activ-

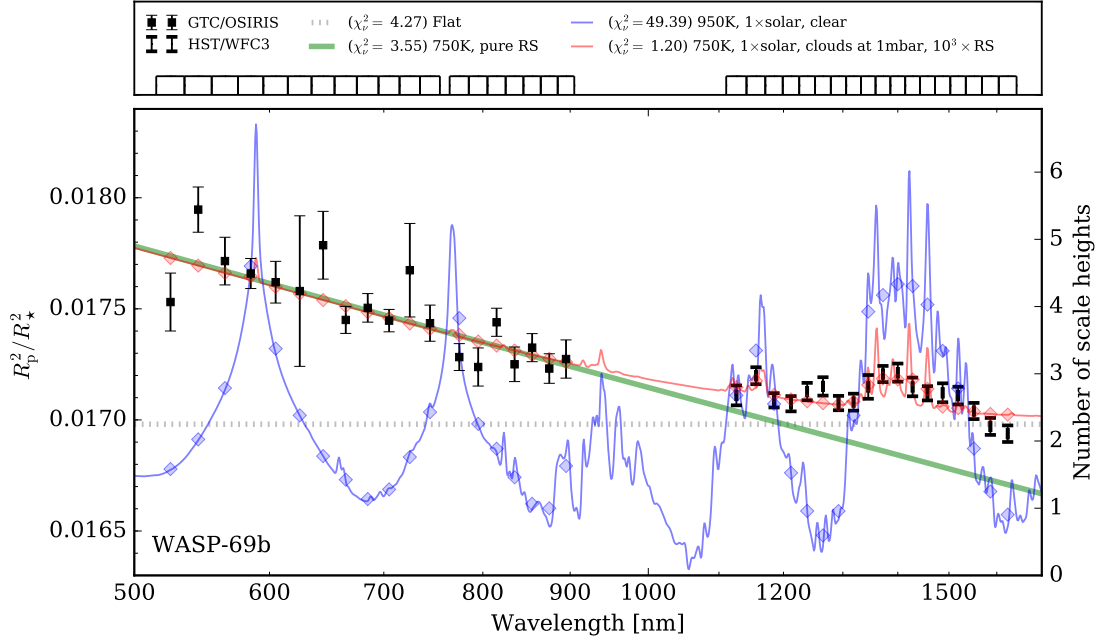


**Fig. 6.** Optical and near infrared transmission spectrum of WASP-69b (black squares) compared with the same theoretical atmosphere models explained in Fig. 5. The near infrared data was obtained using WFC3 (Tsiaras et al. 2018). The WFC3 data have been shifted upwards by a constant value of  $\Delta R_p^2/R_*^2 = 580$  ppm.

ity. If the remaining offset is solely introduced by stellar activity, it would indicate that the flux level at the epoch of the WFC3 observation is  $\sim 2.2\%$  higher than that at the epoch of the OSIRIS observation. The discovery WASP photometry of WASP-69 indeed showed several modulation periods with different amplitudes. The largest semi-amplitude of  $\sim 13$  mmag would allow a flux variation of  $\sim 2.4\%$ , on par with the aforementioned remaining offset.

In the following sections, we compare the observed spectra with theoretical models, to infer the potential atmospheric properties of WASP-69b.

### 5.1. Forward model comparison

We created a grid of transmission spectrum fiducial models using the Exo-Transmit (Kempton et al. 2017) code. The models adopted isothermal temperature profiles, spanning from 450 K to 1450 K in steps of 100 K. The adopted metallicities were  $0.1\times$ ,  $1\times$ ,  $10\times$ ,  $100\times$ ,  $1000\times$  solar. We also considered cloud-free scenarios and clouds at 10, 1, and 0.1 mbar, along with scattering of amplitudes at  $1\times$ ,  $10\times$ ,  $100\times$ ,  $1000\times$ ,  $10000\times$   $H_2$  Rayleigh scattering. We binned the transmission spectrum models into the passbands of the OSIRIS and WFC3 transmission spectra. We compared the observed data to the binned models, allowing the WFC3 data to have an overall offset as the free parameter.

The best-matched model comes from the atmosphere with a temperature of 750 K, a metallicity of  $1\times$  solar, a  $1000\times$  enhanced Rayleigh scattering, and clouds at 1 mbar. Figure 6 shows the observed data compared to this best-matched model ( $\chi_r^2 = 1.20$ ), together with another three models: i) a flat line ( $\chi_r^2 = 4.27$ ), ii) a pure Rayleigh scattering model ( $\chi_r^2 = 3.55$ ), iii) a cloud-free model with  $1\times$  solar metallicity at the equilibrium temperature of  $\sim 950$  K ( $\chi_r^2 = 49.39$ ). The completely cloud-free and the completely cloudy atmosphere models can be ruled out. This indicates that an atmosphere with clouds and enhanced

**Table 4.** Retrieved atmospheric parameters using PLATON models with only atmospheric scattering (i.e. without stellar spots) and for models with atmospheric scattering plus the effect of stellar spots.

Parameter	w/o spots	w/ spots
Planet radius at 1 bar $R'_p$ [ $R_p$ ]	$0.947^{+0.006}_{-0.008}$	$0.945^{+0.007}_{-0.017}$
Temperature $T_p$ [K]	$1227^{+133}_{-164}$	$1203^{+123}_{-429}$
Scattering slope $\alpha$	$-8.9^{+2.1}_{-2.3}$	$-8.3^{+2.6}_{-6.7}$
Scattering amplitude $\log A$	$5.2^{+0.3}_{-0.4}$	$2.4^{+1.4}_{-3.6}$
C/O ratio	$0.37^{+0.19}_{-0.20}$	$0.41^{+0.19}_{-0.20}$
Metallicity $\log Z/Z_\odot$	$2.7^{+0.1}_{-0.2}$	$2.7^{+0.2}_{-0.4}$
Cloud-top pressure $\log P_{\text{top}}$ [Pa]	$2.8^{+1.4}_{-1.7}$	$0.5^{+0.8}_{-0.4}$
Spot temperature $T_{\text{spot}}$ [K]	–	$4244^{+236}_{-171}$
Spot fraction $f_{\text{spot}}$	–	$0.10^{+0.03}_{-0.01}$
WFC3 data offset $\delta_{\text{WFC3}}$ [ppm]	$-479^{+55}_{-58}$	$-618^{+60}_{-47}$

Rayleigh scattering from hazes can explain both optical and near infrared results.

### 5.2. Spectral retrieval analysis

We performed spectral retrieval analysis on the combined OSIRIS+WFC3 transmission spectra using the PLATON (Zhang et al. 2019) code. The latest version 5.0 allows the WFC3 data to have an overall shift as the free parameter. We conducted two runs of retrievals, one assuming atmospheric scattering and no contamination by stellar spots while the other run included scat-

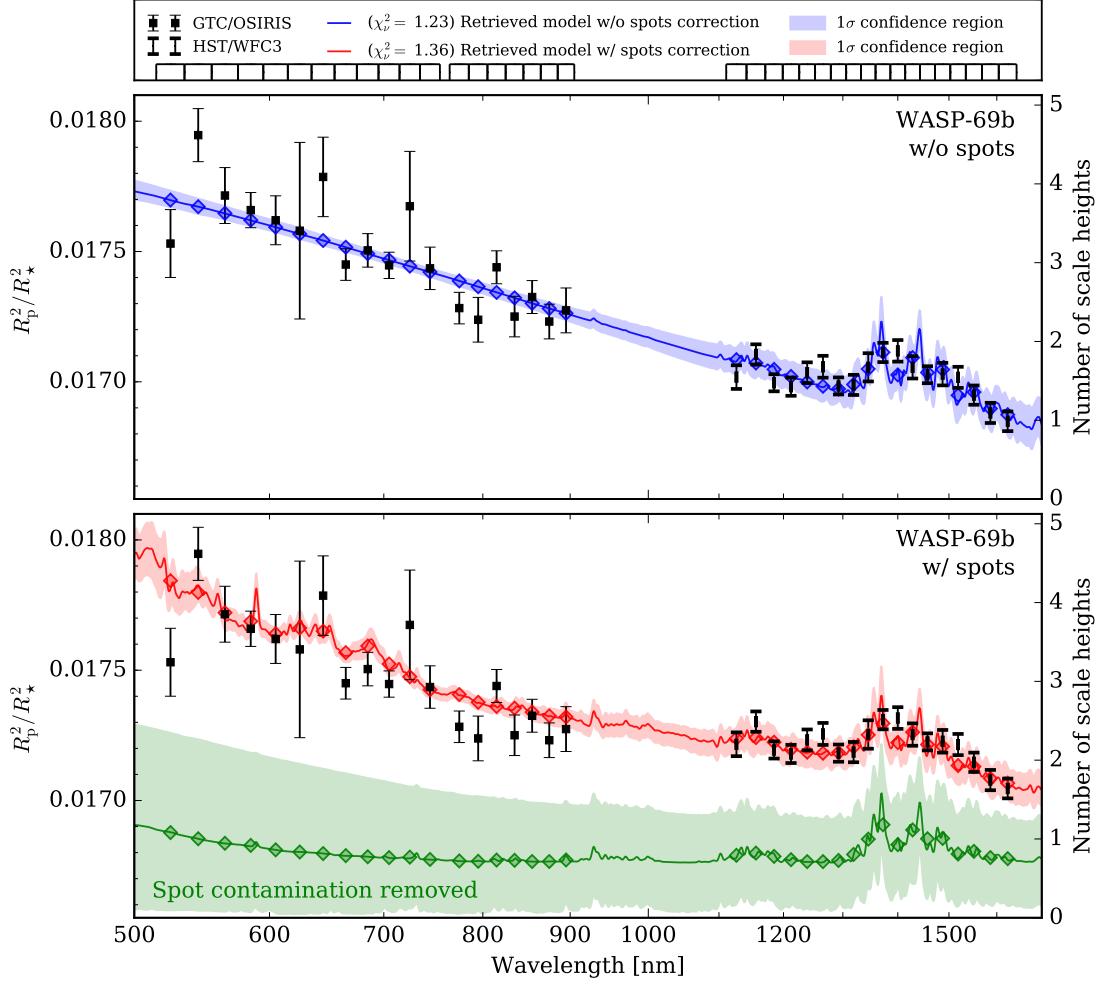


**Fig. 7.** Optical and near infrared transmission spectrum of WASP-69b (black squares) compared with the retrieved models from the PLATON code (Zhang et al. 2019). The shaded area presents the  $1\sigma$  confidence level of the retrieval analysis. *Top panel* shows the legend and the bins of bandpass to derive the transmission spectrum. *Middle panel* shows the retrieval analysis assuming no spots contamination. *Bottom panel* shows the retrieval analysis with spots contamination, where the green model corresponds to the pure planetary atmospheric model after removing the spot contamination from the red model. The WFC3 data (Tsiaras et al. 2018) have been shifted upwards by a constant value of  $\Delta R_p^2/R_*^2 = 479$  ppm (middle panel) and 618 ppm (bottom panel), respectively, which is a free parameter in the retrieval analysis.

tering and the effect of spots. The free parameters include: planet radius at 1 bar ( $R'_p$ ), atmospheric temperature  $T_p$ , C/O ratio, atmospheric metallicity ( $\log Z/Z_\odot$ ), cloud-top pressure ( $\log P_{\text{top}}$ ), scattering slope  $\alpha$ , and scattering amplitude  $\log A$ . In the case of spots correction, the spots are assumed to have a temperature of  $T_{\text{spot}}$  with a filling factor of  $f_{\text{spot}}$ , which assume only one net effect (i.e. spots, or faculae), unlike the separated treatment in Equation 2. We adopted uniform priors for these parameters and employed the nested sampling, implemented by dynesty (Speagle 2020) with 1000 live points, to explore the parameter space. The retrieved results are presented in Table 4 and Figure 7.

Both retrieval runs can fit the observed transmission spectrum reasonably well, and yield a temperature of  $\sim 200$  K higher than the planetary equilibrium temperature ( $T_{\text{eq}} = 963 \pm 18$  K, Anderson et al. 2014). The retrieved metallicity tends to be super-solar, and the retrieved scattering slope is steeper than the nominal Rayleigh scattering slope ( $\alpha = -4$ ). The run with spots correction delivers a spot temperature of  $\Delta T_{\text{phot-spot}} = 456^{+236}_{-171}$  K lower than the stellar photosphere, with a spot coverage of

$0.10^{+0.03}_{-0.01}$ ; i.e., a colder spot temperature and lower spot coverage factor than the values obtained using only the optical data (see Section 4.2).

### 5.3. The atmosphere of WASP-69b

If we assume a molecular weight of  $\mu_m = 2.37$ , our GTC/OSIRIS optical results are consistent with Rayleigh scattering caused by the presence of hydrogen in the atmosphere of WASP-69b. Since WASP-69 is an active star, it is also feasible that the observed slope is solely caused by stellar activity in the form of spots and faculae. If unocculted spots are causing the slope seen in the optical transmission spectrum there could be a detectable extra absorption at the Na I doublet, however according to our spot and faculae modeling that extra absorption is of the order of our measured planet-to-star radius ratio uncertainties.

Combining our optical results with a previously published HST/WFC3 near infrared transmission spectrum, we made two modeling tests: forward model comparison and spectral retrieval.



With forward modeling comparison we can rule out the completely cloud-free or completely cloudy models. Spectral retrieval (with and without considering the effect of stellar spots) seems to suggest that extra sources for scattering (i.e., hazes) and super-solar metallicity can explain the observed slope (and atmospheric features in general) in both wavelength regimes. Hence, there is a possible physical solution that indicates that the detected Rayleigh scattering signal can come from the planet's atmosphere. Both derived transmission spectra (optical and NIR) present a slope compatible with Rayleigh scattering, if this slope is caused by stellar activity in the form of unocculted spots that would mean that the spot coverage was more or less similar during both observations. The HST/WFC3 data were taken on 16th of August 2016 (Proposal ID 14260, P. I. Drake Deming) while the GTC/OSIRIS data were taken on 5th of October 2016, roughly 50 days apart or close to twice the rotational period of WASP-69 ( $P_{\text{rot}} = 23$  days, [Anderson et al. 2014](#)). Studies performed on other active planet-host stars found spot life cycles between 60 to 90 days (Kepler-210, a K-type star, [Ioannidis & Schmitt 2016](#)), and even evidence for longer lifetimes (75 to 330 days, Kepler-17, G2V star, [Bonomo & Lanza 2012](#)); the possibility that both observations were affected by the same (or a similar) group of spots present in the surface of WASP-69 can not be ruled out.

At the time of writing this paper, the optical and near infrared transmission spectrum of HAT-P-12b was announced by [Wong et al. \(2020\)](#). HAT-P-12b is a sub-Saturn mass transiting planet orbiting a K dwarf discovered by [Hartman et al. \(2009\)](#). This planet possesses a mass, radius, and orbital period ( $M_p = 0.21 M_{\text{Jup}}$ ,  $R_p = 0.96 R_{\text{Jup}}$ ,  $P = 3.21$  days) similar to WASP-69b ( $M_p = 0.26 M_{\text{Jup}}$ ,  $R_p = 1.05 R_{\text{Jup}}$ ,  $P = 3.86$  days); although HAT-P-12b orbits around a star with sub-solar metallicity ( $[\text{Fe}/\text{H}] = -0.29$  dex) and WASP-69 metallicity is super-solar ( $[\text{Fe}/\text{H}] = 0.15$  dex). The optical and near infrared transmission spectrum of HAT-P-12b looks remarkably similar to WASP-69b, with a slope consistent with Rayleigh scattering in the optical and a water absorption feature at  $1.4 \mu\text{m}$ . Based on their photometric follow-up, [Wong et al. \(2020\)](#) argue that HAT-P-12 is a very quiescent star with low photometric variability and conclude that the observed optical slope in the spectrum is likely originated from the planetary atmosphere. In contrast, WASP-69 seems to exhibit higher levels of stellar activity as indicated by the  $\log R'_{\text{HK}}$  index ( $\log R'_{\text{HK}} \sim -4.54$ , [Anderson et al. 2014](#) compared to HAT-P-12  $\log R'_{\text{HK}} = -4.90$  [Mancini et al. 2018](#)) and in the form of photometric variability as shown in the discovery paper of this system. Still, their retrieved transmission spectra look identical.

## 6. Conclusions

We present here the results of the analysis of one primary transit of the Saturn-mass exoplanet WASP-69b taken on 5th of October 2016 with the long-slit spectrograph OSIRIS mounted on GTC (10.4 m). We observed WASP-69 and one reference star simultaneously during  $\sim 3.5$  hours. Using their spectra we were able to integrate the flux of both stars and created several light curves using differential spectrophotometry.

We searched for evidence of Na absorption originating from the planetary atmosphere of WASP-69b creating light curves with central bands centered around the Na I doublet. The transmission spectrum around the Na lines is mostly flat, with no signs of extra absorption at the center of the Na doublet and with no signs of broad absorption line wings. However, the expected

Na I features reported in previous studies are probably below our detection limits.

The observed optical transmission spectrum presents a slope of increasing planet-to-star radius ratio towards blue wavelengths. Using the equation that links the change of apparent planetary radius versus wavelength and atmospheric scale height, assuming that the atmosphere of WASP-69b is hydrogen-dominated ( $\mu_m = 2.37$ ) and adopting a planetary temperature of  $T_{\text{eq}} = 963 \pm 18$  K and a planetary surface gravity of  $\log g_p = 2.726 \pm 0.046$  (cgs), we find  $\alpha = -3.35 \pm 0.75$ . This value is consistent with Rayleigh scattering produced by hydrogen. Since WASP-69 is an active star, it is possible that the observed slope is caused by unocculted spots and faculae. Modeling the amount of area covered and temperatures of spots and faculae necessary to reproduce our optical data, we find filling factors of  $\delta_{\text{spot}} = 0.55^{+0.30}_{-0.27}$  and  $\delta_{\text{facu}} = 0.15^{+0.46}_{-0.13}$  and temperatures  $T_{\text{spot}} = 4594^{+48}_{-77}$  K and  $T_{\text{facu}} = 4788^{+308}_{-68}$  K for spots and faculae respectively.

We combined our optical GTC/OSIRIS measurements with a previously published HST/WFC3 near infrared transmission spectrum. We compared the full set (optical plus near infrared spectrum) with different atmospheric models, we can rule out completely cloud-free or completely cloudy models to explain the observations. Our spectral retrieval analysis (including the effect of stellar spots) suggests that extra sources for scattering and super-solar metallicity models can explain the main optical and near infrared features of the transmission spectrum of WASP-69b.

Based on the previously reported slope found in the HST/WFC3 transmission spectrum of WASP-69b and the previously reported atmospheric escape of He, the lack of any spot-crossing features in our white-light transit light curve and our atmospheric model comparison, we speculate that the slope seen in our data is more likely to be caused by hazes present in the atmosphere of WASP-69b rather than caused by stellar active regions. However, we can not completely rule out the possibility that the detected signal is indeed produced by stellar activity, hence independent observations of the system with other instruments at different epochs should help to confirm or reject this interpretation.

**Acknowledgements.** Based on observations made with the Gran Telescopio Canarias (GTC), installed in the Spanish Observatorio del Roque de los Muchachos of the Instituto de Astrofísica de Canarias, in the island of La Palma. G. C. acknowledges the support by the Natural Science Foundation of Jiangsu Province (Grant No. BK20190110), the National Natural Science Foundation of China (Grant No. 11503088, 11573073, 11573075), and the Minor Planet Foundation of the Purple Mountain Observatory.

**Software:** ipython ([Pérez & Granger 2007](#)), numpy ([van der Walt et al. 2011](#)), scipy ([Jones et al. 2001](#)), matplotlib ([Hunter 2007](#)). This research made use of Astropy, a community-developed core Python package for Astronomy ([Astropy Collaboration et al. 2013](#), [Astropy Collaboration et al. 2018](#)). Correlation plots for spot modeling done with Corner ([Foreman-Mackey 2016](#)).

## References

- Alexoudi, X., Mallonn, M., von Essen, C., et al. 2018, *A&A*, 620, A142
- Ambikasaran, S., Foreman-Mackey, D., Greengard, L., Hogg, D. W., & O'Neil, M. 2015, *IEEE Transactions on Pattern Analysis and Machine Intelligence*, 38, 252
- Anderson, D. R., Collier Cameron, A., Delrez, L., et al. 2014, *MNRAS*, 445, 1114
- Astropy Collaboration, Price-Whelan, A. M., Sipőcz, B. M., et al. 2018, *AJ*, 156, 123
- Astropy Collaboration, Robitaille, T. P., Tollerud, E. J., et al. 2013, *A&A*, 558, A33
- Benneke, B. & Seager, S. 2012, *ApJ*, 753, 100
- Bixel, A., Rackham, B. V., Apai, D., et al. 2019, *AJ*, 157, 68

- Bonomo, A. S. & Lanza, A. F. 2012, A&A, 547, A37
- Casasayas-Barris, N., Pallé, E., Nowak, G., et al. 2017, A&A, 608, A135
- Casasayas-Barris, N., Pallé, E., Yan, F., et al. 2018, A&A, 616, A151
- Casasayas-Barris, N., Pallé, E., Yan, F., et al. 2019, A&A, 628, A9
- Cepa, J., Aguiar, M., Escalera, V. G., et al. 2000, in Proc. SPIE, Vol. 4008, Optical and IR Telescope Instrumentation and Detectors, ed. M. Iye & A. F. Moorwood, 623–631
- Charbonneau, D., Brown, T. M., Noyes, R. W., & Gilliland, R. L. 2002, ApJ, 568, 377
- Chen, G., Casasayas-Barris, N., Pallé, E., et al. 2020, A&A, 635, A171
- Chen, G., Guenther, E. W., Pallé, E., et al. 2017a, A&A, 600, A138
- Chen, G., Pallé, E., Nortmann, L., et al. 2017b, A&A, 600, L11
- Chen, G., Pallé, E., Welbanks, L., et al. 2018, A&A, 616, A145
- Deibert, E. K., de Mooij, E. J. W., Jayawardhana, R., et al. 2019, AJ, 157, 58
- Eastman, J., Siverd, R., & Gaudi, B. S. 2010, PASP, 122, 935
- Espinoza, N. & Jordán, A. 2015, MNRAS, 450, 1879
- Foreman-Mackey, D. 2016, The Journal of Open Source Software, 1, 24
- Foreman-Mackey, D., Hogg, D. W., Lang, D., & Goodman, J. 2013, PASP, 125, 306
- Gaia Collaboration. 2018, VizieR Online Data Catalog, I/345
- Gibson, N. P., Aigrain, S., Roberts, S., et al. 2012, MNRAS, 419, 2683
- Hartman, J. D., Bakos, G. Á., Torres, G., et al. 2009, ApJ, 706, 785
- Heng, K. & Kitzmann, D. 2017, MNRAS, 470, 2972
- Høg, E., Fabricius, C., Makarov, V. V., et al. 2000, A&A, 355, L27
- Horne, K. 1986, PASP, 98, 609
- Hunter, J. D. 2007, Computing In Science & Engineering, 9, 90
- Husser, T. O., Wende-von Berg, S., Dreizler, S., et al. 2013, A&A, 553, A6
- Ioannidis, P. & Schmitt, J. H. M. M. 2016, A&A, 594, A41
- Jones, E., Oliphant, T., Peterson, P., et al. 2001, SciPy: Open source scientific tools for Python, [Online; accessed <today>]
- Jordán, A., Espinoza, N., Rabus, M., et al. 2013, ApJ, 778, 184
- Kempton, E. M. R., Lupu, R., Owusu-Asare, A., Slough, P., & Cale, B. 2017, PASP, 129, 044402
- Kreidberg, L. 2015, PASP, 127, 1161
- Kreidberg, L., Bean, J. L., Désert, J.-M., et al. 2014, Nature, 505, 69
- Kurucz, R. L. 1979, ApJS, 40, 1
- Lecavelier Des Etangs, A., Pont, F., Vidal-Madjar, A., & Sing, D. 2008, A&A, 481, L83
- Mancini, L., Esposito, M., Covino, E., et al. 2018, A&A, 613, A41
- Mandel, K. & Agol, E. 2002, ApJ, 580, L171
- May, E. M., Gardner, T., Rauscher, E., & Monnier, J. D. 2020, AJ, 159, 7
- May, E. M., Zhao, M., Haidar, M., Rauscher, E., & Monnier, J. D. 2018, AJ, 156, 122
- McCullough, P. R., Crouzet, N., Deming, D., & Madhusudhan, N. 2014, ApJ, 791, 55
- Murgas, F., Chen, G., Pallé, E., Nortmann, L., & Nowak, G. 2019, A&A, 622, A172
- Nortmann, L., Pallé, E., Salz, M., et al. 2018, Science, 362, 1388
- Oshagh, M., Santos, N. C., Ehrenreich, D., et al. 2014, A&A, 568, A99
- Pérez, F. & Granger, B. E. 2007, Computing in Science and Engineering, 9, 21
- Pont, F., Sing, D. K., Gibson, N. P., et al. 2013, MNRAS, 432, 2917
- Rackham, B., Espinoza, N., Apai, D., et al. 2017, ApJ, 834, 151
- Rackham, B. V., Apai, D., & Giampapa, M. S. 2018, ApJ, 853, 122
- Rackham, B. V., Apai, D., & Giampapa, M. S. 2019, AJ, 157, 96
- Rasmussen, C. & Williams, C. 2010, the MIT Press, 122, 935
- Redfield, S., Endl, M., Cochran, W. D., & Koesterke, L. 2008, ApJ, 673, L87
- Sánchez, B., Aguiar-González, M., Barreto, R., et al. 2012, in Proc. SPIE, Vol. 8446, Ground-based and Airborne Instrumentation for Astronomy IV, 84464T
- Seidel, J. V., Ehrenreich, D., Wyttenbach, A., et al. 2019, A&A, 623, A166
- Sing, D. K., Fortney, J. J., Nikolov, N., et al. 2016, Nature, 529, 59
- Sing, D. K., Huitson, C. M., Lopez-Morales, M., et al. 2012, MNRAS, 426, 1663
- Sing, D. K., Pont, F., Aigrain, S., et al. 2011, MNRAS, 416, 1443
- Speagle, J. S. 2020, MNRAS, 493, 3132
- Todorov, K. O., Désert, J.-M., Huitson, C. M., et al. 2019, A&A, 631, A169
- Tsiaras, A., Waldmann, I. P., Zingales, T., et al. 2018, AJ, 155, 156
- van der Walt, S., Colbert, S. C., & Varoquaux, G. 2011, Computing in Science and Engineering, 13, 22
- Weaver, I. C., López-Morales, M., Espinoza, N., et al. 2020, AJ, 159, 13
- Wong, I., Benneke, B., Gao, P., et al. 2020, AJ, 159, 234
- Wood, P. L., Maxted, P. F. L., Smalley, B., & Iro, N. 2011, MNRAS, 412, 2376
- Wyttenbach, A., Lovis, C., Ehrenreich, D., et al. 2017, A&A, 602, A36
- Zhang, M., Chachan, Y., Kempton, E. M. R., & Knutson, H. A. 2019, PASP, 131, 034501

**Table A.1.** Results for the planet-to-star radius ratio for each of the 19 spectroscopic channels.

Center (nm)	Width (nm)	$R_p/R_\star$
525	20	$0.132403^{+0.000446}_{-0.000539}$
545	20	$0.133965^{+0.000386}_{-0.000374}$
565	20	$0.133097^{+0.000351}_{-0.000455}$
585	20	$0.132887^{+0.000260}_{-0.000249}$
605	20	$0.132740^{+0.000352}_{-0.000355}$
625	20	$0.132589^{+0.001475}_{-0.001080}$
645	20	$0.133365^{+0.000603}_{-0.000541}$
665	20	$0.132099^{+0.000234}_{-0.000226}$
684	20	$0.132304^{+0.000255}_{-0.000231}$
705	20	$0.132087^{+0.000194}_{-0.000188}$
725	20	$0.132943^{+0.000728}_{-0.000855}$
745	20	$0.132043^{+0.000310}_{-0.000307}$
775	20	$0.131464^{+0.000239}_{-0.000221}$
795	20	$0.131294^{+0.000427}_{-0.000226}$
815	20	$0.132059^{+0.000242}_{-0.000237}$
835	20	$0.131341^{+0.000283}_{-0.000310}$
855	20	$0.131626^{+0.000242}_{-0.000238}$
875	20	$0.131268^{+0.000255}_{-0.000252}$
895	20	$0.131431^{+0.000346}_{-0.000309}$

**Table A.2.** Results for the planet-to-star radius ratio for each of the 11 spectroscopic channels around the Na I doublet.

Center (nm)	Width (nm)	$R_p/R_\star$
564.3	5	$0.133100^{+0.000501}_{-0.000473}$
569.3	5	$0.133121^{+0.000431}_{-0.000484}$
574.3	5	$0.132683^{+0.000483}_{-0.000527}$
579.3	5	$0.133343^{+0.000419}_{-0.000425}$
584.3	5	$0.133790^{+0.000467}_{-0.000444}$
589.3	5	$0.129845^{+0.001861}_{-0.002393}$
594.3	5	$0.132244^{+0.000484}_{-0.000457}$
599.3	5	$0.131914^{+0.000418}_{-0.000416}$
604.3	5	$0.132476^{+0.000442}_{-0.000447}$
609.3	5	$0.133244^{+0.001299}_{-0.001218}$
614.3	5	$0.130494^{+0.002538}_{-0.001250}$

## Appendix A: Additional tables and figures

Here we present the transmission spectrum measurement tables, the correlation plots of the MCMC fitting procedure of spots and faculae modeling, and the transmission spectrum around the Na doublet region.

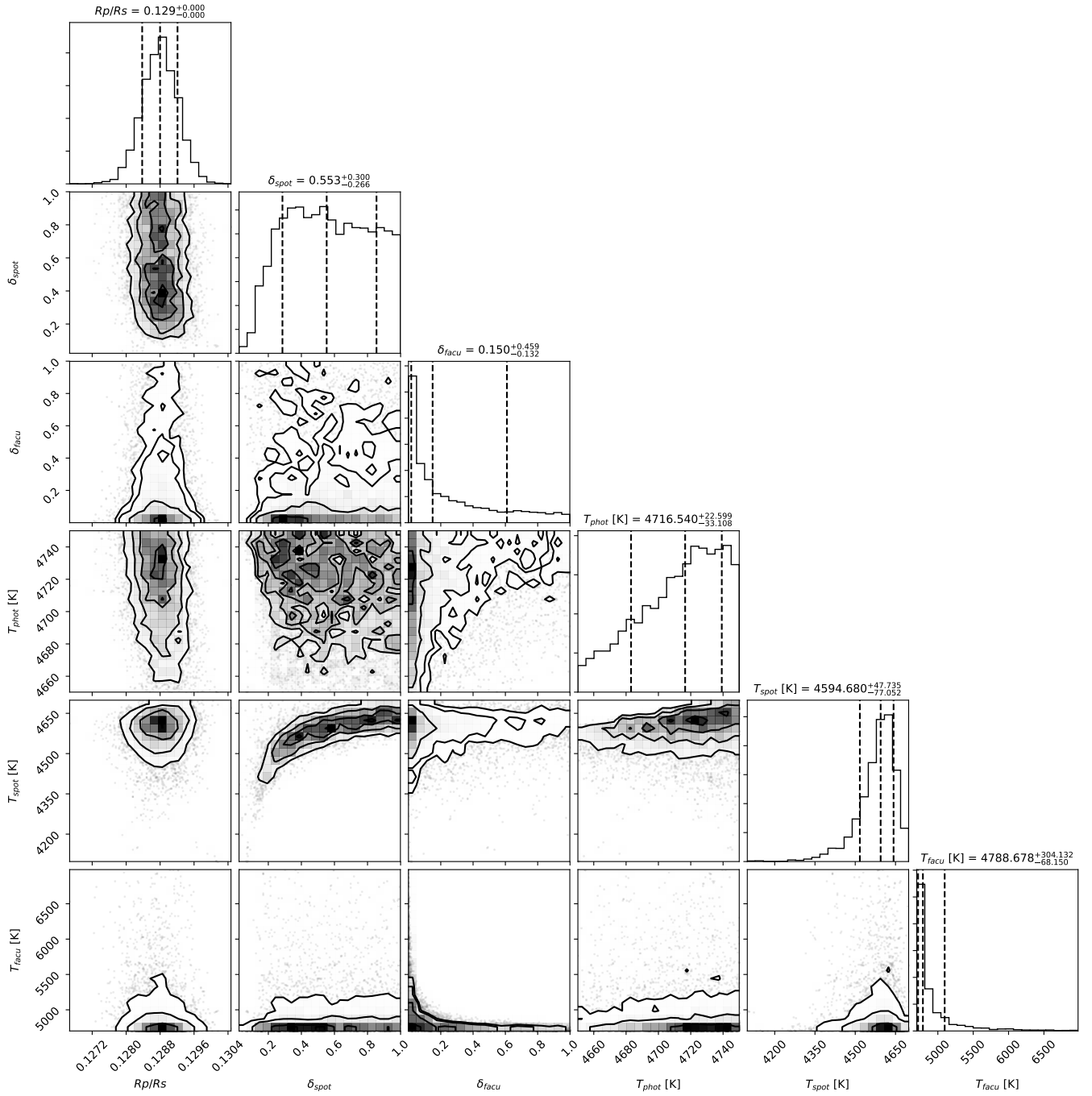


**Fig. A.1.** Correlation plot of fitted parameters for the spot and faculae coverage model.



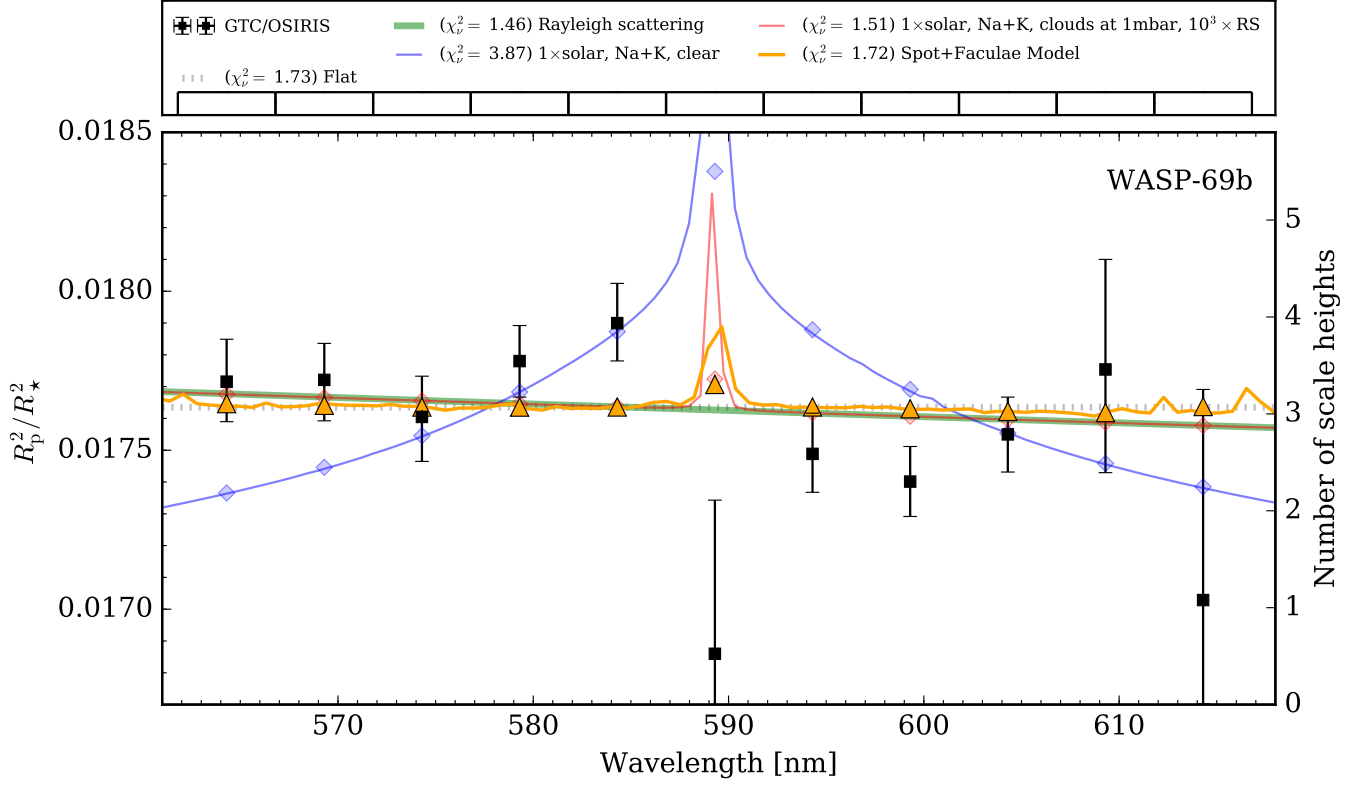


**Fig. A.2.** Transmission spectrum of WASP-69b around the Na I doublet (black squares) compared to several atmosphere models. In blue a model for a clear atmosphere and solar abundance is shown. The grey dashed line indicates a the model of flat transmission spectrum. The slope expected in an atmospheres affected solely by Rayleigh scattering is shown in green. In red we show the model of an atmosphere with clouds at 1 mbar and Rayleigh scattering enhanced by a factor of 1000. In orange the best fitted unocculted spots and faculae model is shown.